Research Square

Preprints are preliminary reports that have not undergone peer review.
They should not be considered conclusive, used to inform clinical practice,
or referenced by the media as validated information.

Photocatalytic Nitrogen Fixation over Copper-Modified Bismuth Molybdate

Hongfan Zhai
Jiangsu University of Technology
Qinjing Feng
Jiangsu University of Technology
Yang Zhao
Jiangsu University of Technology
Jiawang Liu
Jiangsu University of Technology
Xueer Wei
Jiangsu University of Technology
Youting Zhang
Jiangsu University of Technology
Fengli Yang
yangfengli1984@hotmail.com
Jiangsu University of Technology

Research Article

Keywords: Ammonia synthesis, Photocatalysis, Cu-doped, Bismuth molybdate

Posted Date: May 25th, 2026

DOI: https://doi.org/10.21203/rs.3.rs-9687863/v1

License: This work is licensed under a Creative Commons Attribution 4.0 International License.
Read Full License

Additional Declarations: No competing interests reported.

Version of Record: A version of this preprint was published at Brazilian Journal of Chemical Engineering on August 17th, 2026. See the published version at https://doi.org/10.1007/s43153-026-00706-z.

Abstract

Ammonia is an indispensable industrial feedstock, yet its conventional Haber-Bosch ammonia synthesis remains heavily reliant on energy-intensive high-temperature and high-pressure conditions. Photocatalytic nitrogen fixation offers a sustainable alternative by utilizing abundant solar energy under mild ambient conditions. Herein, the effects of metal ion modifications on the photocatalytic nitrogen fixation and ammonia synthesis performance of bismuth molybdate (BMO) under simulated solar irradiation were systematically investigated. Notably, the Cu-doped BMO exhibited superior catalytic activity, achieving a remarkable ammonia evolution rate of 115.78 umol g^{-1} under simulated sunlight. Comprehensive characterizations, including BET, UV-vis DRS, and electrochemical analyses, revealed that the Cu modification endows the catalyst with an enlarged specific surface area thereby providing more active sites for subsequent reactions, a broadened optical absorption range the bandgap narrows, and the concentration of oxygen vacancies increases, and an optimized band structure. Furthermore, based on the detailed analysis of the structural and photoelectrochemical properties, the underlying mechanism responsible for the enhanced photocatalytic performance induced by metal ion modification was elucidated.

1. Introduction

Ammonia is not only an indispensable chemical feedstock for producing various industrial chemicals, such as fertilizers, but also serves as a crucial clean energy carrier and fuel.(Zhang, Ward et al. 2020, Deshmukh, Kamble et al. 2024, Yu, Wang et al. 2025). Currently, the Haber-Bosch process remains the dominant method for industrial NH_3 synthesis. However, this process is heavily dependent on harsh reaction conditions, including high temperatures (450–500 ^oC) and elevated pressures (> 200 atm), which culminate in enormous energy consumption and severe environmental issues(Li 2018, Run Shi 2019, Zuo, Su et al. 2023). Consequently, it is highly imperative to explore sustainable alternatives for NH_3 synthesis.

In recent years, photocatalytic nitrogen fixation technology has emerged as a promising alternative, owing to its distinct advantages of mild operating conditions, eco-friendliness, energy conservation, and sustainability(Xu, Qiu et al. 2018, Chen, Shou et al. 2023, Li, Wang et al. 2023, Tian, Zhao et al. 2024). However, this process is impeded by several intrinsic challenges. The N_2 molecule, characterized by an ultra-high bond energy (941 kJ/mol) and a nonpolar structure, poses formidable obstacles to its chemisorption and activation(Xiao, Wang et al. 2019, Chen, Liu et al. 2020).. Simultaneously, the rapid recombination of photogenerated carriers severely limits the improvement of quantum efficiency(Ithisuphalap, Zhang et al. 2018, Run Shi 2019, Ting Sun 2024, Donghui Cui 2025), while the six-electron reduction process required for photocatalytic N_2 fixation suffers from a high kinetic energy barrier(Wu, Tan et al. 2019). Collectively, these factors contribute to the generally suboptimal efficiency of current photocatalytic nitrogen fixation systems(Yunxuan Zhao 2022).Consequently, the central

bottleneck of overcoming these limitations lies in the rational design of highly efficient and robust photocatalysts.

Among various candidates, BMO has attracted extensive attention due to its appropriate band structure, non-toxicity, eco-friendliness, low cost, abundance, and high stability(Liu, Li et al. 2023, Chuanjiao Wang 2024, Zhenyu Liu 2024). However, the application of BMO in photocatalytic nitrogen fixation is plagued by multiple critical bottlenecks. Primarily, the lack of effective active sites on its surface results in exceedingly weak N_2 adsorption and activation, rendering the cleavage of the inert N ≡ N triple bond formidable. Furthermore, from a kinetic perspective, the severe recombination and ultrashort lifetime of charge carriers fail to sustain the sluggish six-electron transfer process. Finally, its inherent bandgap restricts the solar spectrum absorption range, leading to suboptimal light utilization. Collectively, these issues result in the intrinsically poor nitrogen reduction activity of BMO(Taoxia Ma 2023). Among the commonly employed modification strategies, metal doping stands out due to its inherent advantages in tuning electronic and band structures, enhancing intrinsic activity, and broadening the light absorption range, thereby exhibiting superior photocatalytic performance(Zeng, Liu et al. 2021, Shen, Shou et al. 2022, Zhang, Li et al. 2022). The efficacy of this structural modulation has been demonstrated across various photocatalytic applications For instance, Muhammad et al.(Waqar, Imran et al. 2019) synthesized La-doped BMO photocatalysts using a sol-gel method with sodium dodecyl sulfate as a surfactant for methylene blue degradation. It was found that the La-doped BMO exhibited a 10% improvement in the degradation efficiency of methylene blue. Mechanistically, La doping induced a morphological transformation of BMO from dense rods to highly porous clustered spherical particles, which contributed to the enhanced catalytic performance.

To date, investigations into metal ion-modified BMO for photocatalytic ammonia synthesis remain relatively scarce. Herein, this study systematically explored the effects of various metal ion dopants on the nitrogen fixation and ammonia synthesis performance of BMO. The results indicated that, compared with undoped BMO, the Cu, Ti, Co, and Sn-modified BMO samples exhibited superior catalytic activities, achieving ammonia evolution rates of 115.78, 108.66, 90.46 and 85.77 umol g^{-1} under simulated sunlight, respectively. By combining comprehensive characterizations (BET, UV-vis, and electrochemical analyses), the underlying mechanism for the enhanced catalytic performance of metal ion-modified BMO was proposed.

2. Materials and Methods

2.1 Preparation of Catalysts

Preparation of metal ion-doped bismuth molybdate: 2 mmol of $Bi(NO_3)_3 \cdot 5H_2O$ and 1 mmol of $Na_2MoO_4 \cdot 2H_2O$ were dissolved separately in 30 mL of ethylene glycol. The Na_2MoO_4 solution was slowly added dropwise into the $Bi(NO_3)_3$ solution under stirring. After stirring for 5 minutes, a certain amount of the corresponding nitrate or chloride solution was added, and stirred for 1 h. The resulting transparent

solution was transferred into a 100 mL Teflon-lined stainless-steel autoclave and maintained at 160 ^{o}C for 12 h, followed by cooling to room temperature. The final product was collected by filtration, washed with water and ethanol, and dried at 60 ^{o}C for 12 h to obtain the metal ion-modified BMO.

2.2 Characterization of Catalysts

The crystal structure of the catalysts was characterized using an X'PERT POWDER X-ray diffractometer (XRD). Fourier transform infrared (FT-IR) spectra were recorded on Bruker Tensor 27 spectrometer over the range of 500–4000 cm^{-1} with a resolution of 4 cm^{-1}. The elemental composition and chemical states were analyzed via X-ray photoelectron spectroscopy (XPS, AXIS U1tra DLD). The micromorphology was examined using a Sigma 500 field-emission scanning electron microscope (SEM). N_2 physisorption isotherms were measured at -196 ^{o}C using a fully automated analyzer to determine the specific surface area and pore size distribution. Furthermore, the ultraviolet-visible diffuse reflectance spectra (UV-vis DRS) and photoluminescence (PL) spectra were acquired using a Hitachi UV-3010 UV-vis spectrophotometer and an FLS920 fluorescence spectrometer, respectively. Finally, to evaluate the photoelectrochemical properties of the materials, photocurrent responses and electrochemical impedance spectroscopy (EIS) were measured on a CHI660B electrochemical workstation employing a standard three-electrode system.

2.3 Evaluation of Photocatalytic Performance for Ammonia Synthesis

Photocatalytic N_2 reduction experiment: A 300 W Xenon lamp equipped with an AM 1.5 filter was used as the light source. Firstly, 25 mg of catalyst was added into a quartz reactor containing 200 mL of a 5% methanol solution. The system was purged with high-purity nitrogen (50 mL/min) and pre-treated in the dark for 30 minutes. Subsequently, the Xenon lamp was turned on, and the reactor temperature was maintained constant by circulating water. Samples were collected at specific time intervals (every 30 min), and the ammonia content was analyzed using a Nessler agent colorimetric method.

3. Results and Discussion

3.1 Photocatalytic nitrogen fixation performance

The nitrogen fixation performance of various metal-ion-doped bismuth molybdate (BMO) samples was evaluated under simulated sunlight irradiation, and the results are presented in Fig. 1. As shown in Fig. 1a, after 120 min of reaction, the NH_3 yields of Cu-BMO, Co-BMO, Ti-BMO, and Sn-BMO reached 115.78, 108.66, 90.46, and 85.77 umol g^{-1}, respectively. In contrast, the undoped BMO exhibited a lower NH_3 evolution rate of 82.63 umol g^{-1}. These results indicate that the doping of Cu, Co, Ti, and Sn effectively enhances the photocatalytic N_2 fixation performance.

This enhancement can be attributed to a synergistic combination of several factors. Firstly, ion metal doping typically leads to an increased specific surface area, which provides a higher density of surface catalytic active sites for N_2 adsorption and reaction. Secondly, the introduced impurity energy levels effectively inhibit the rapid recombination of photogenerated electron-hole pairs, thereby prolonging the lifetime of charge carriers. Most importantly, as evidenced in related studies, metal doping induces the formation of oxygen vacancies (OVs) within the BMO lattice. These OVs serve as active sites that significantly enhance the chemisorption and activation capabilities for the inert N_2 molecules, ultimately lowering the energy barrier for the N ≡ N bond cleavage and boosting the overall nitrogen fixation performance(Sharma, Kumar et al. 2023, Taoxia Ma 2023, Li, Bao et al. 2025).

Furthermore, the photocatalytic performance under full-spectrum and visible-light (λ > 420 nm) irradiation was compared (Fig. 1c). Notably, the nitrogen fixation efficiency of all catalysts under visible light was markedly lower than that under full-spectrum light. This indicates that ultraviolet (UV) light plays a decisive role in this system. This observation is consistent with the optical absorption properties of the catalysts, which primarily absorb UV light, as will be corroborated by the photogenerated charge carrier separation results discussed later in Fig. 8a.

The durability and stability of photocatalysts are key factors for evaluating their practical application performance. After five consecutive cycling tests, Cu-BMO exhibited a marginal decrease in catalytic activity, which may be primarily attributed to catalyst loss during the recovery process. Furthermore, the slight activity decay may also stem from minor agglomeration induced by repeated recycling operations, which adversely affects the specific surface area and the availability of active sites. Nevertheless, Cu-BMO still exhibited relatively stable nitrogen reduction performance Fig. 2(a).

To verify the source of the generated ammonia, controlled photocatalytic experiments were conducted under various reaction conditions (Fig. 2(b)). The absence of detectable NH_3 in either catalyst-free systems or under an Ar atmosphere unambiguously confirms that the measured ammonia originates exclusively from the catalytic reduction of N_2. Furthermore, the reliability of the quantification was cross-validated using both Nessler's reagent and the indophenol blue methods (Fig. 2(c)) The resulting concentrations exhibited agreement with the indophenol blue method yielding marginally lower values. Considering the complex reaction network of photocatalytic N_2 fixation, where the formation of N_2H_4 often serves as a competing side reaction, product selectivity was systematically evaluated (Fig. 2(d)) The negligible N_2H_4 yield indicates that the intermediate species were rapidly converted, confirming the high selectivity toward NH_3 of the Cu-BMO catalysts.

3.2 Structure and Morphology Characterization

The crystal structure of the as-prepared samples was characterized by XRD analysis. As depicted in Fig. 3(a), the distinct diffraction peaks of the undoped BMO at 28.27°, 32.47°, 36.75°, 46.72°, and 55.6° can be well-indexed to the (131), (200), (151), (202), and (331) crystal planes of orthorhombic Bi_2MoO_6 (JCPDS No. 77-1246). Notably, following Cu doping, no discernible diffraction peaks corresponding to Cu

species or secondary phases are detected, indicating that the introduction of Cu does not disrupt the inherent lattice of BMO. However, a careful examination reveals a systematic shift of the (131) peak toward lower angles with increasing Cu content (Fig. 3(b)). This distinct lattice expansion unambiguously confirms the successful incorporation of Cu ions into the BMO crystal lattice. Furthermore, the Cu-BMO samples exhibit an obvious broadening in the full width at half maximum (FWHM) compared to pristine BMO. This phenomenon suggests a reduced crystallite size, which could be reasonably ascribed to the lattice distortion and the consequent strain induced by the insertion of heterogeneous Cu ions(Mingnv Guo 2026).

Figure 4 presents the FTIR spectra of the BMO and Cu-doped BMO samples. For BMO, the characteristic absorption bands located between 400 and 900 cm^{-1} are primarily associated with the Bi-O, Mo-O, and Mo-O-Mo bridging stretching and bending vibrations. Specifically, the prominent band at 815 cm^{-1} is assigned to the symmetric stretching mode of the MoO_6 octahedra (involving apical oxygen atoms), whereas the peak at 733 cm^{-1} corresponds to the asymmetric stretching vibrations of the oxygen atoms within these octahedra. Additionally, the bands at 547 and 465 cm^{-1} could be ascribed to the bending vibrations and the coupled stretching-bending modes of the MoO_6 units, respectively. Notably, the FTIR profiles of Cu-BMO exhibit negligible variation compared to those of BMO. This high spectral similarity is likely due to the extremely low Cu doping concentration (0.12%), which exerts a minimal turbulence on the chemical bond polarity and the local electronic structure of the host material.

Figure 5 (a) presents the SEM images of BMO, revealing that the sample consists of microspheres with diameters ranging from 1 to 3 μm. These microspheres are constructed by densely packed nanosheets and nanoparticles, forming a rough hierarchical architecture. This specific morphology is highly desirable as it provides a large specific surface area and abundant active sites, which are crucial for facilitating the photocatalytic nitrogen fixation reaction(Liu, Li et al. 2023, Xiong, Peng et al. 2024).

Following Cu doping (Fig. 5(b)), the overall microspherical morphology and hierarchical structure are well preserved. However, a closer inspection at a higher magnification (20,000×) reveals that the constituent building blocks become noticeably smaller and more discretely dispersed. Furthermore, the EDS elemental mapping of Cu-BMO (Fig. 5(c, d)) demonstrates a relatively uniform spatial distribution of Bi, Mo, O, and Cu elements throughout the microspheres, which concurrently confirms the successful incorporation of Cu ions into the BMO.

The pore structure and specific surface area of the samples were evaluated via N_2 adsorption-desorption isotherms. As shown in Fig. 6, both samples exhibit type IV isotherms with distinct H3 hysteresis loops at a relative pressure (P/P_0) range of 0.6-1.0. This indicates the presence of a mesoporous structure, which is well-supported by the corresponding pore size distribution curves. Furthermore, the undoped BMO possesses a specific surface area of 22.84 $m^2 \cdot g^{-1}$ and an N_2 adsorption capacity of 80.67 $cm^3 \cdot g^{-1}$. Following Cu doping, these values increase to 27.26 $m^2 \cdot g^{-1}$ and 92.67 $cm^3 \cdot g^{-1}$, respectively. This enhancement in textural properties could be attributed to the reduced particle size and looser packing

architecture observed in the SEM images (Fig. 5). Ultimately, the enlarged specific surface area and enhanced N_2 adsorption capacity of Cu-BMO create more favorable conditions for mass transfer and the subsequent surface catalytic reduction of N_2.

3.3 Chemical composition

To elucidate the surface chemical composition and elemental states, XPS characterization was conducted on both BMO and Cu-BMO. As depicted in Fig. 7(b), the Bi 4f spectrum of BMO displays two strong peaks at 159.1 eV and 164.8 eV, corresponding to Bi 4f $_{7/2}$ and Bi 4f $_{5/2}$, respectively. Similarly, the Mo 3d $_{5/2}$ and Mo 3d $_{3/2}$ signals of BMO are located at 232.1 eV and 235.5 eV (Fig. 7c). Notably, following Cu doping, while the overall spectral profiles remain largely consistent, indicating the preservation of the primary valence states, and the characteristic peaks for both Bi and Mo in Cu-BMO synchronously shift toward higher binding energies. This systematic shift indicates the successful Cu incorporation into the lattice, where the substitution-induced electronic interaction causes an electron density decrease in the neighboring Bi and Mo atoms(Sharma, Kumar et al. 2023) (Mingnv Guo 2026).

Furthermore, the O 1s XPS spectra (Fig. 7(d)) can be deconvoluted into three peaks at 531.8, 530.8, and 529.9 eV, which are assigned to surface hydroxyl groups, oxygen vacancies (O_v), and lattice oxygen, respectively. The introduction of Cu, with its distinct ionic radius, inevitably triggers lattice distortion. This structural deformation destabilizes local chemical bonds, thereby promoting the generation of abundant O_v on the catalyst surface(Zhang, Zhang et al. 2022). Ultimately, these structural and electronic modulations synergize that the optimized electronic structure facilitates the separation of photogenerated charge carriers and improves the adsorption energy of intermediates, while the enriched O_v serve as highly active sites to effectively capture and activate inert N_2 molecules. Together, they significantly boost the overall photocatalytic nitrogen fixation performance(Zhang, Gu et al. 2021, Li, Kong et al. 2026, Zhenke Fan 2026).3.4 Optical property

UV-vis diffuse reflectance spectroscopy (DRS) was employed to investigate the optical properties of the catalysts. As illustrated in Fig. 8 (a), the absorption edge of the undoped BMO was located at approximately 490 nm. Upon Cu doping, the absorption edge of the catalyst exhibited a distinct red shift, indicating an enhanced visible light absorption capability of the Cu-BMO catalyst(Chandrappa, Galbao et al. 2023). The UV-vis DRS data were transformed into bandgap energy plots using the Kubelka-Munk function (Fig. 8 (b)). The narrowing of the bandgap following Cu doping could be primarily attributed to the increased concentration of oxygen vacancies(Mingnv Guo 2026) Such modification improved the optical properties of the photocatalyst, facilitating the generation of electron-hole pairs and consequently promoting the photo response process(Li, Zhou et al. 2020). Figure 8 (c) displays the valence band (VB) XPS spectra of the samples, where the x-axis intercept indicates the position of the VB. The VB potentials of BMO and Cu-BMO were determined to be 2.14 and 2.16 eV, respectively. By combining the Eg and VB values derived from VB-XPS and UV-vis DRS, the corresponding electronic band structures were constructed (Fig. 8 (d)). Based on the experimentally determined bandgap values, the CB potentials of BMO and Cu-BMO were calculated to be -0.17 and − 0.09 eV, respectively. Notably,

compared to undoped BMO, the CB edge of Cu-BMO undergoes an upward shift towards more positive potentials, which is consistent with both experimental characterizations and theoretical calculations. Although this positive shift is thermodynamically unfavorable for the reduction of N_2, it does not compromise the overall nitrogen reduction performance. Instead, the remarkably enhanced activity can be attributed to the synergistic effects of accelerated charge transfer, abundant oxygen vacancies, and an enlarged specific surface area. These factors collectively drive ultrafast charge separation dynamics and robust N_2 adsorption, effectively overcoming the thermodynamic limitation.

3.4 Electrochemical Performance Analysis

Electrochemical impedance spectroscopy (EIS) was conducted to evaluate the charge transfer and separation efficiency of the catalysts (Fig. 9(a)). Notably, Cu-BMO exhibited a significantly smaller semicircle in the Nyquist plot, indicating a lower charge transfer resistance compared to BMO. This reduction in resistance reflects a decreased transport barrier for photogenerated charge carriers within the material bulk. Such unimpeded charge migration pathways effectively suppress electron-hole recombination and prolong carrier lifetime. Consequently, a larger population of active photogenerated charges could efficiently enrich at the catalyst surface to drive the reaction, thereby significantly enhancing the overall photocatalytic efficiency.(Pradhan, Bariki et al. 2024, Hou, Han et al. 2025) .

Figure 9(b) presents the photoluminescence (PL) spectra of BMO and Cu-BMO. Notably, a significant quenching of the PL peak intensity is observed upon Cu doping. This decrease in fluorescence emission indicates the effective suppression of photogenerated electron-hole recombination, demonstrating that the introduction of Cu species profoundly prolongs the charge carrier lifetime and facilitates their spatial separation and transport.

Figure 9 (c) displays the photocurrent response curves of BMO and Cu-BMO. The Cu-doped BMO demonstrated a higher photocurrent response, directly indicating superior charge separation efficiency, which is consistent with the PL and EIS analyses. Notably, both samples exhibit characteristic transient spikes followed by a gradual decay upon both illumination onset and interruption. This distinctive charging and discharging profile resembles the behavior of a pseudo capacitor(Wang, Wang et al. 2012). Physically, this phenomenon reflects the rapid accumulation and subsequent depletion of photogenerated electrons at the electrode/electrolyte interface. At the mechanistic level, this behavior can be attributed to the dynamic electron mediator role played by the doped Cu ions. Specifically, the Cu active sites facilitate a continuous electron capture-release cycle through reversible valence state variations: under illumination, photogenerated electrons are initially captured by high-valence Cu ions (Cu^{2+}) and reduced to low-valence states (Cu^{+}); subsequently, these reduced species transfer the trapped electrons to the reaction substrates (e.g., N_2), concurrently being re-oxidized to their initial high-valence states(Li, Bao et al. 2025).Collectively, the PL, EIS, and transient photocurrent analyses consistently demonstrate that Cu doping optimizes the charge carrier dynamics of the catalyst. By effectively prolonging the charge carrier lifetime and reducing the charge transfer resistance, Cu-BMO

establishes a highly efficient internal charge transport network, which serves as the fundamental driving force for its remarkably enhanced photocatalytic nitrogen fixation performance.

Figure 10(a) presents the cyclic voltammetry (CV) curves of the catalysts scanned at a rate of 120 mV s^{-1}, where Cu-BMO exhibits the highest current density, consistent with the EIS results. To quantitatively evaluate the electrochemically active surface area (ECSA), CV measurements were performed at various scan rates ranging from 20 to 120 mV s^{-1} (Fig. 10(b)). As depicted in Fig. 10(c), the capacitive current differences (Δj) were plotted against the scan rates. The significantly steeper slope obtained for Cu-BMO indicates a substantially larger ECSA compared to BMO. This expansion in active area can be attributed to the introduction of heterovalent Cu ions, which generates abundant active sites that are highly favorable for the adsorption and activation of H_2O and N_2 molecules.

4. Conclusions

In summary, a series of metal-ion-doped BMO photocatalysts were successfully fabricated via a hydrothermal route, with Cu-BMO exhibiting the most pronounced enhancement in photocatalytic N_2 fixation. Systematic characterizations reveal that Cu doping triggers multi-dimensional optimization of the catalyst. Morphologically, it induces a looser architecture, enlarging the specific surface area and enriching mesoporous structures, which boosts the adsorption capacity for N_2 molecules. Electronically, the introduction of Cu species narrows the bandgap for extended visible-light harvesting, while the generated oxygen vacancies and heterovalent Cu ions act as dynamic electron mediators. This synergistic structural and electronic modulation establishes an efficient charge migration network, as evidenced by significantly suppressed carrier recombination and accelerated charge transfer. Ultimately, the combined effects of robust reactant adsorption, enhanced light absorption, and optimized charge kinetics synergistically contribute to the ammonia synthesis activity of Cu-BMO.

Declarations

Conflict of interest

The authors have no conflict of interest.

Author Contribution

Y.F. conceived the project and supervised the work, Z.H.designed and conducted the experiments and analyzed the data and wrote the manuscript, F.Q. and Z.Y. assisted in the synthesis and optimization of the photocatalysts, L.J. performed the photoelectrochemical measurements , W.X. and Z.Y. carried out the structural and morphological characterizations (XRD, TEM, XPS, etc.) and visualized the data. All authors discussed the results and contributed to the final manuscript.

Acknowledgements

This research was partially supported by Postgraduate Practice Innovation Program of Jiangsu University of Technology (No. XSJCX24_98, XSJCX25_104).

Data availability

The data from this investigation are contained in the paper. Further inquiries should be made to the corresponding author.

References

1. Chandrappa S, Galbao SJ, Furube A, Murthy DHK (2023) Extending the Optical Absorption Limit of Graphitic Carbon Nitride Photocatalysts: A Review. Acs Appl Nano Mater 6(21):19551–19572
2. Chen LC, Shou JX, Chen YT, Han WH, Tu XW, Zhang LP, Sun Q, Cao J, Chang YR, Zheng H (2023) Efficient sunlight promoted nitrogen fixation from air under room temperature and ambient pressure via Ti/Mo composites. Chem Eng J 451
3. Chen S, Liu D, Peng T (2020) Fundamentals and Recent Progress of Photocatalytic Nitrogen-Fixation Reaction over Semiconductors. Solar RRL 5(2)
4. Chuanjiao Wang SW, Ping Y, Zhao Z, Guo D, Wang D, Bu X (2024) Ru@MIL-125_MnOx metal-organic-framework-based cocatalysts for photocatalytic nitrogen fixation. Environment and Energy, Applied Catalysis B
5. Deshmukh SP, Kamble SJ, Koli VB (2024) Recent Advances in Application of 1D Nanomaterials for Photocatalytic Nitrogen Fixation. Nitrogen 5(2):349–372
6. Donghui Cui XY, Liu Y, Li M, ChunxueWang F, Li (2025) Direct Z-scheme heterojunctions with perylenetetracarboxylic diimide decorated amino-rich porous g-C3N4 nanosheets for metal-free photocatalytic N2 fixation Separation and Purification Technology
7. Hou DR, Han L, Hou ZY, Yang ZR, Lu TL, Si XQ, Liu X, Li JR, Luo WB, Wang JF (2025) Dynamic Oxygen Vacancy Formation via Photoexcitation in Sn-Modified Defective BiOCl Nanoflowers for Enhanced Photocatalytic Nitrogen Fixation. ACS Catal 15(24):20947–20957
8. Ithisuphalap K, Zhang H, Guo L, Yang Q, Yang H, Wu G (2018) Photocatalysis and Photoelectrocatalysis Methods of Nitrogen Reduction for Sustainable Ammonia Synthesis. Small Methods 3(6)
9. Li MH, Wang LB, Li FY, Xu L (2023) Construction of Co3O4 nanopolyhedra with rich oxygen vacancies from ZIF-67 for efficient photocatalytic nitrogen fixation. Photochem Photobiol Sci 22(6):1233–1243
10. Li P, Zhou Z, Wang Q, Guo M, Chen S, Low J, Long R, Liu W, Ding P, Wu Y, Xiong Y (2020) Visible-Light-Driven Nitrogen Fixation Catalyzed by Bi(5)O(7)Br Nanostructures: Enhanced Performance by

Oxygen Vacancies. J Am Chem Soc 142(28):12430–12439

11. Li R (2018) Photocatalytic nitrogen fixation: An attractive approach for artificial photocatalysis. Chin J Catal 39(7):1180–1188
12. Li YL, Bao R, Kong X, Liu L, Ge ZH, Liu F, Cui H, Yi JH (2025) Synergistic engineering of Oxygen Vacancies and strain in Sn-doped bismuth molybdate for enhanced photocatalytic nitrogen fixation. J Alloys Compd 1046
13. Li YL, Kong X, Bao R, Liu L, Ge ZH, Liu F, Cui H, Yi JH (2026) Robust oxygen vacancy surfaces induce chemical bonding interfaces of Bi2Sn2O7/Bi2MoO6 S-scheme heterojunction with asymmetric adsorption sites for efficient photocatalytic nitrogen fixation. Chem Eng J 531
14. Liu Z, Li X, Su S, Ding W, Meng L, Wang Y, Tan M, Luo M (2023) Enhancing photocatalytic nitrogen fixation performance of Co-doped bismuth molybdate through band engineering tuning. Appl Surf Sci 611
15. Mingnv Guo YC, Liu J, Qiu J, Wang W, Yang Z (2026) Thermally assisted photocatalysis_ oxygen vacancy-mediated enhanced photothermal synergistic CO2 reduction over Cu-Ni Co-doped Bi2MoO6. Applied Surface Science
16. Pradhan SK, Bariki R, Nayak SK, Panda S, Das NK, Mishra BG (2024) Facile Synthesis of Oxygen-Deficient CeVO4/Bi/Bi2MoO6 Ternary Heterostructures with Bi-Mediated Switching from Type-I to Z-Scheme Mechanism for O2 and N2 Photoreductions. Ind Eng Chem Res 63(40):17193–17206
17. Run Shi YZ, Geoffrey N, Waterhouse S, Zhang T, Zhang (2019) Defect Engineering in Photocatalytic Nitrogen Fixation.
18. Sharma M, Kumar A, Gill D, Jaiswal S, Patra A, Bhattacharya S, Krishnan V (2023) Boosting Photocatalytic Nitrogen Fixation via Nanoarchitectonics Using Oxygen Vacancy Regulation in W-Doped Bi(2)MoO(6) Nanosheets. ACS Appl Mater Interfaces 15(48):55765–55778
19. Shen YF, Shou JX, Chen LC, Han WH, Zhang LP, Chen YT, Tu XW, Zhang SF, Sun Q, Chang YR, Zheng H (2022) Efficient photocatalytic nitrogen fixation from air under sunlight via iron-doped WO3. Applied Catalysis a-General 643
20. Taoxia Ma CY, Li Guo RAS, Wang D, Xu BFeng Fu (2023) Refining electronic properties of Bi2MoO6 by In-doping for boosting overall nitrogen fixation via relay catalysis. Environmental, Applied Catalysis B
21. Tian JR, Zhao ZX, Ling HQ, Zhang ZQ, Ablat H, Nurmamat X (2024) Review on photocatalytic nitrogen fixation by local surface plasmon. Int J Hydrog Energy 87:686–698
22. Ting Sun PG, He Y, Liu ZWJXinshan Rong (2024) Dual Z-scheme TCN_ZnS_ ZnIn2S4 with efficient separation for photocatalytic nitrogen fixation. Journal of Colloid and Interface Science
23. Wang Y, Wang X, Antonietti M (2012) Polymeric graphitic carbon nitride as a heterogeneous organocatalyst: from photochemistry to multipurpose catalysis to sustainable chemistry. Angew Chem Int Ed Engl 51(1):68–89
24. Waqar M, Imran M, Adil SF, Noreen S, Latif S, Khan M, Siddiqui MRH (2019) Enhanced Photoluminescence and Photocatalytic Efficiency of La-Doped Bismuth Molybdate: Its Preparation

and Characterization. Materials (Basel) 13(1)

25. Wu S, Tan X, Liu K, Lei J, Wang L, Zhang J (2019) TiO2 (B) nanotubes with ultrathin shell for highly efficient photocatalytic fixation of nitrogen. Catal Today 335:214–220
26. Xiao C, Wang H, Zhang L, Sun S, Wang W (2019) Enhanced Photocatalytic Nitrogen Fixation on MoO2/BiOCl. Compos ChemCatChem 11(24):6467–6472
27. Xiong SH, Peng T, Huang LL, Wang R, He BB, Jin J, Wang HW, Gong YS (2024) Synthesis and characterization of Ag/Cu dual-metal-functionalized porous Bi2WO6 microsphere with enhanced N2 photofixation. J Alloys Compd 1004
28. Xu C, Qiu P, Li L, Chen H, Jiang F, Wang X (2018) Bismuth Subcarbonate with Designer Defects for Broad-Spectrum Photocatalytic Nitrogen Fixation. ACS Appl Mater Interfaces 10(30):25321–25328
29. Yu XR, Wang YC, Ding J, Li Z, He B, Zeng ZW, Zhu PX, Xu XR, Liu XY, Wang H, Wang Y (2025) Doping induced diatomic active sites over MoO3-x for efficient and stable photocatalytic N2 reduction to ammonia. Chem Eng J 504
30. Yunxuan Zhao YM, Zhou C, Zhang T (2022) Artificial photocatalytic nitrogen fixation: Where are we now？. Where is its future？. Molecular Catalysis
31. Zeng H, Liu L, Zhang D, Wang Y, Li Z, Liu C, Zhang L, Cui X (2021) Fe(III)-C3N4 hybrids photocatalyst for efficient visible-light driven nitrogen fixation. Mater Chem Phys 258
32. Zhang X, Ward BB, Sigman DM (2020) Global Nitrogen Cycle: Critical Enzymes, Organisms, and Processes for Nitrogen. Budgets Dynamics Chem Reviews 120(12):5308–5351
33. Zhang Y, Gu S, Zhou XY, Gao KY, Sun K, Wu D, Xia JJ, Wang XF (2021) Boosted photocatalytic nitrogen fixation by bismuth and oxygen vacancies in Bi2MoO6/BiOBr composite structures. Catal Sci Technol 11(14):4783–4792
34. Zhang Y, Zhang J, Yi Q, Wang F, Fu H, Gao H, Liao Y (2022) In Situ Construction of Porous β-Bi2O3/BiOCOOH Heterojunction Photocatalysts: Enhancing Nitrogen Fixation Activity by the Synergistic Effect of Oxygen Vacancies and Lattice Oxygen. ACS Appl Energy Mater 5(8):9503–9511
35. Zhang ZP, Li FF, Li GQ, Li R, Wang YF, Wang YW, Zhang XC, Zhang LL, Li FF, Liu JX, Fan CM (2022) Cu-doped MIL-101(Fe) with enhanced photocatalytic nitrogen fixation performance. J Solid State Chem 310
36. Zhenke Fan HLKG, Deng Q, Xia Y, Liu a S, Hou YZW (2026) Structural transformation promoted oxygen vacancy creation and spatial separation of vacancies and holes in bismuth molybdate boost photocatalytic nitrogen fixation and stability. Journal of Catalysis
37. Zhenyu Liu ML, Cao Y, Meng L, Yang Y, Li X (2024) Tuning the electronic properties of Bi2MoO6 by S-doping to boost efficient photocatalytic nitrogen fixation reactions. Journal of Catalysis
38. Zuo C, Su Q, Yu L (2023) Res Progress Compos Mater Photocatalytic Nitrogen Fixation Molecules 28(21)

Figures

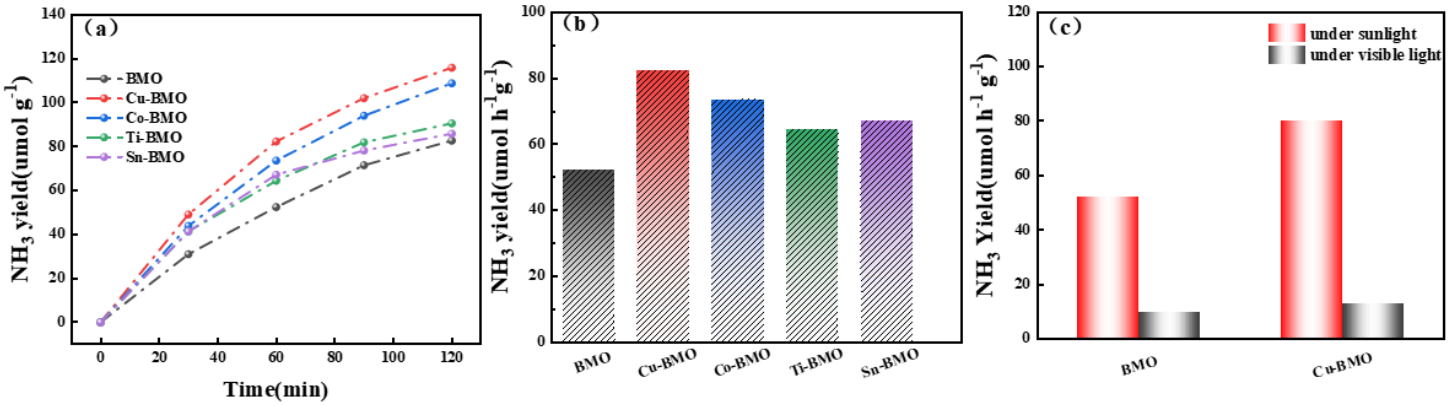


Figure 1

(a) Ammonia production rates of different catalysts under simulated solar irradiation; (b) Ammonia yield of the catalyst within 60 min under simulated solar irradiation; (c) Ammonia production under different light irradiation conditions.

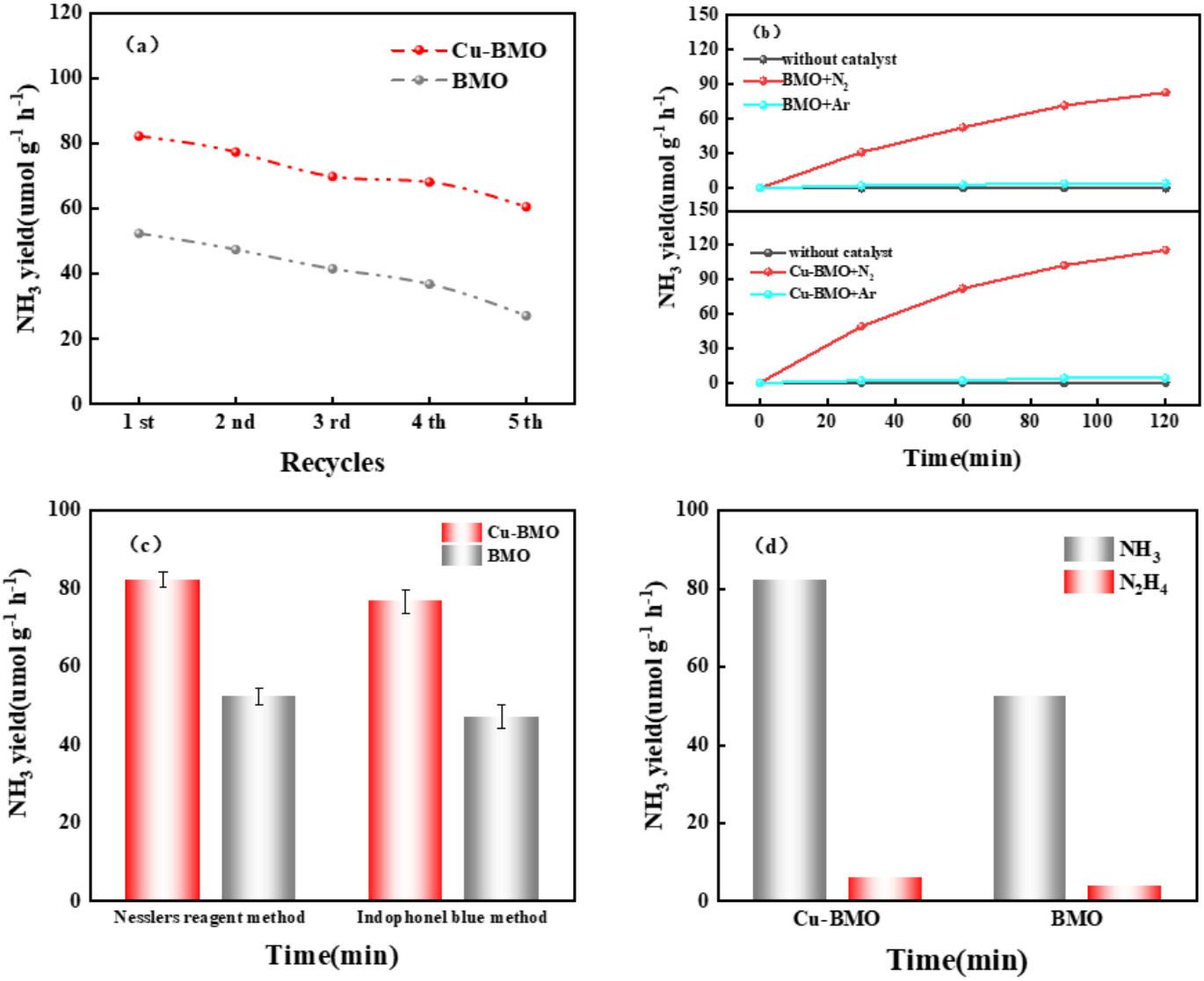


Figure 2

(a) Cycling stability results of Cu-BMO; (b) Experimental results under different conditions; (c) comparison of different detection methods; (d) Products selectivity results ..

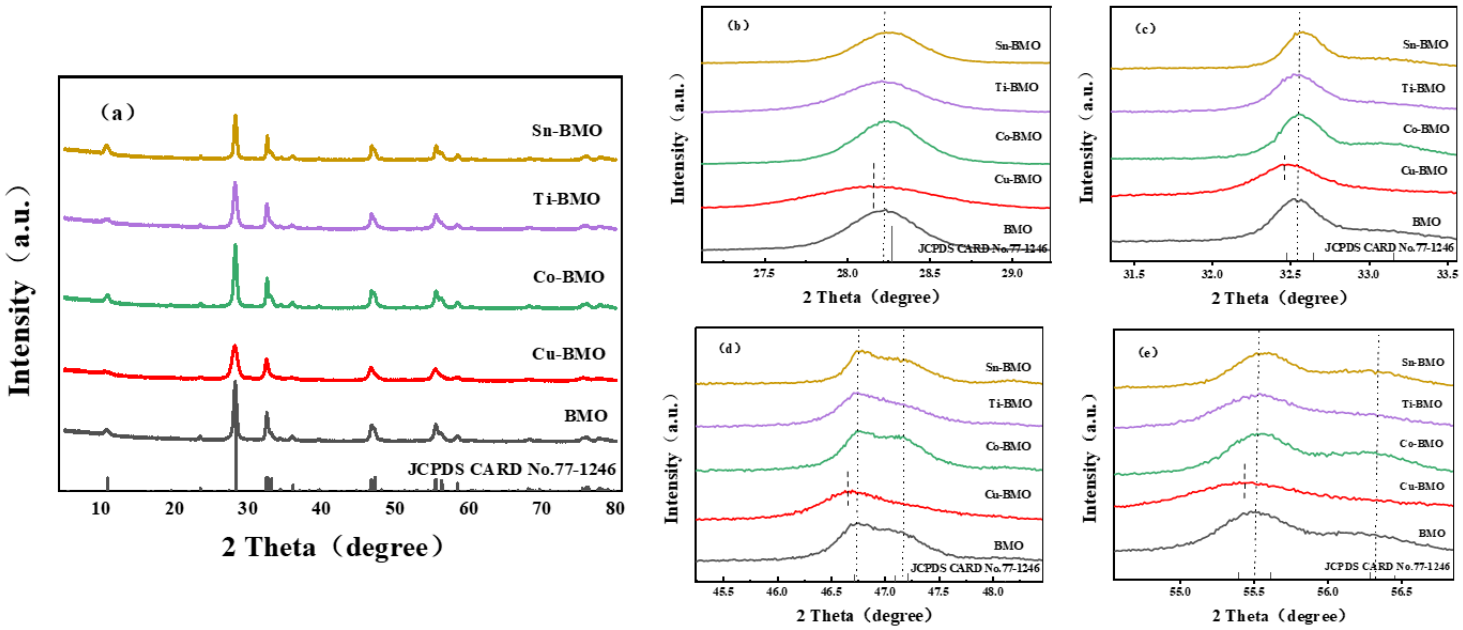


Figure 3

(a-e) XRD patterns of BMO and various metal-ion-doped BMO samples. Locally magnified views of the XRD patterns at different diffraction angles.

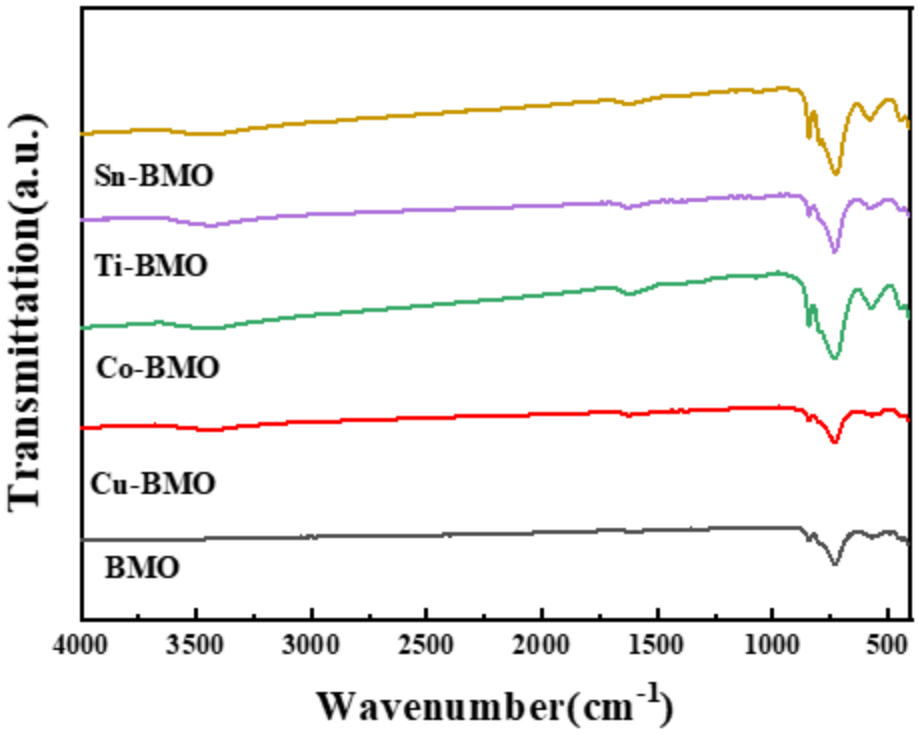


Figure 4

FTIR spectra of BMO and BMO doped with different metal ions

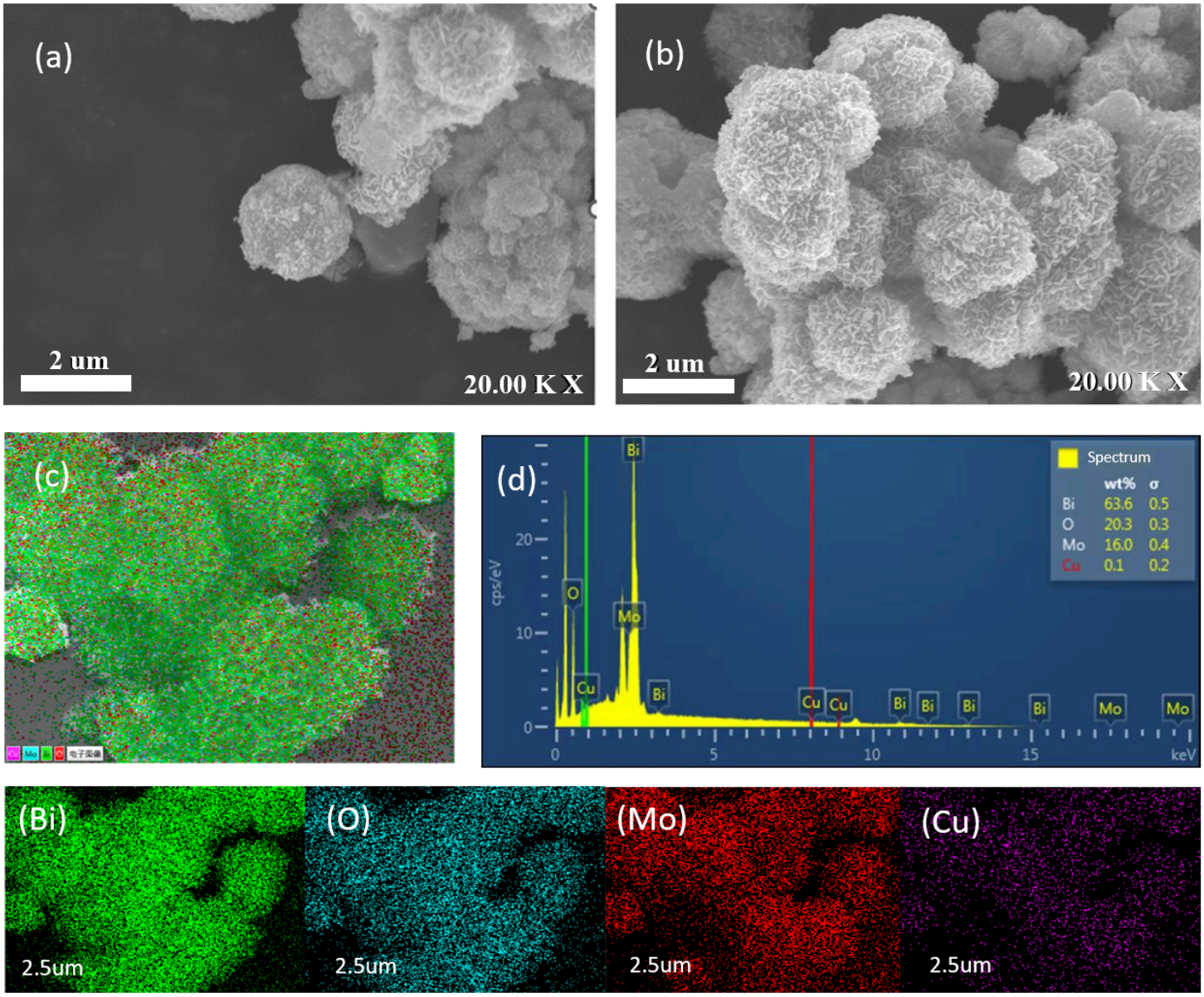


Figure 5

SEM images of BMO (a) and Cu-BMO (b), respectively; (c-d) EDS mapping and EDS Spectrum of Cu-BMO.

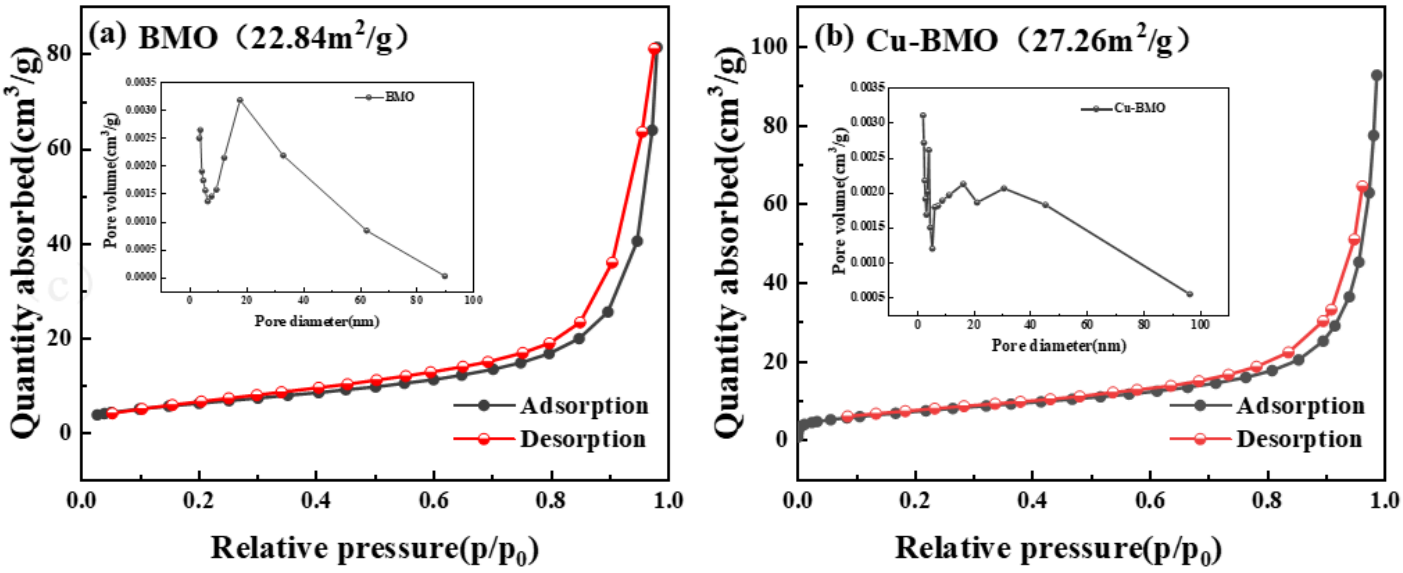


Figure 6

(a, b) BET results of BMO and Cu-BMO, respectively.

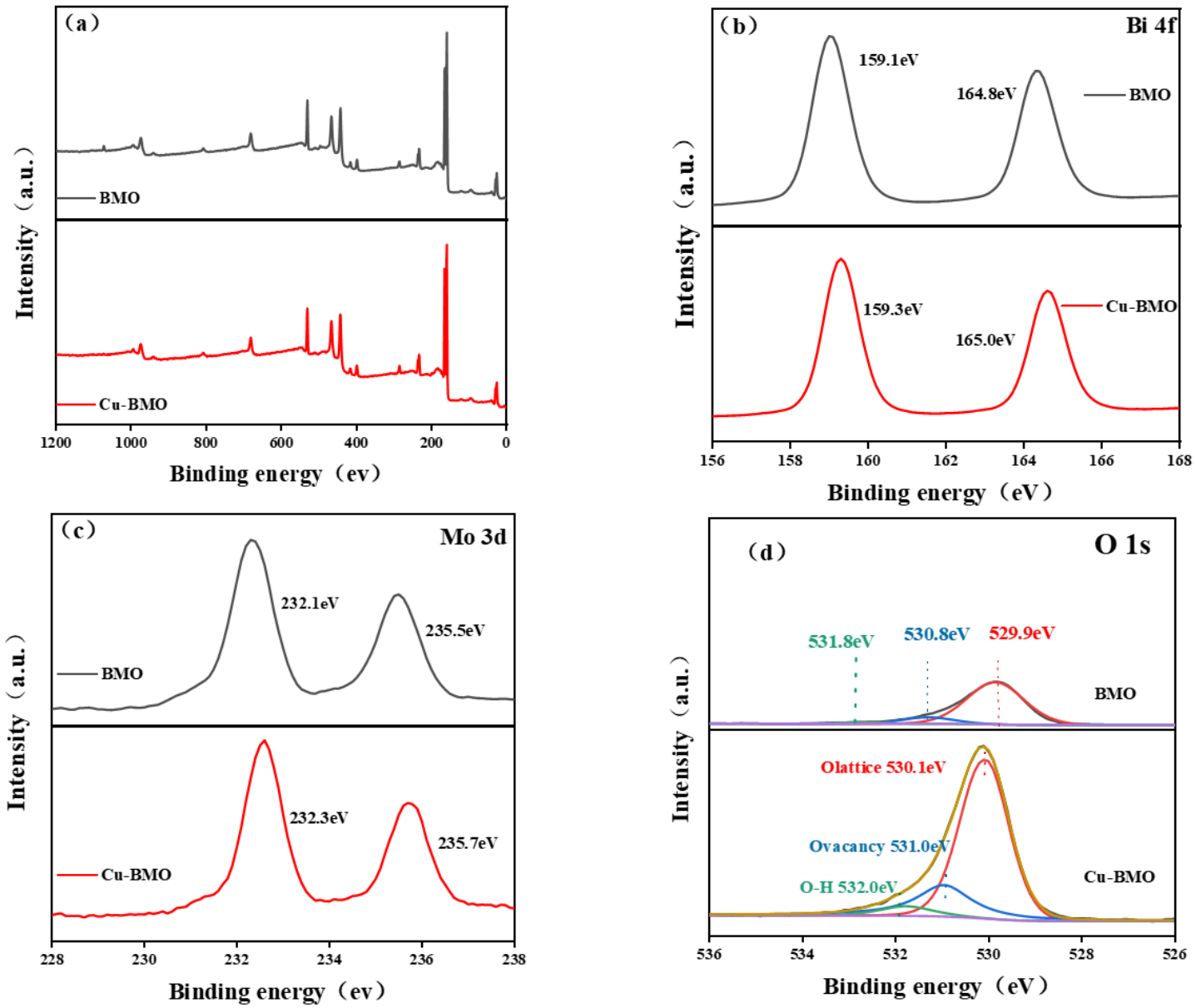


Figure 7

(a) XPS survey spectrum; (b) Bi 4f; (c) Mo 3d; (d) O 1s XPS spectra

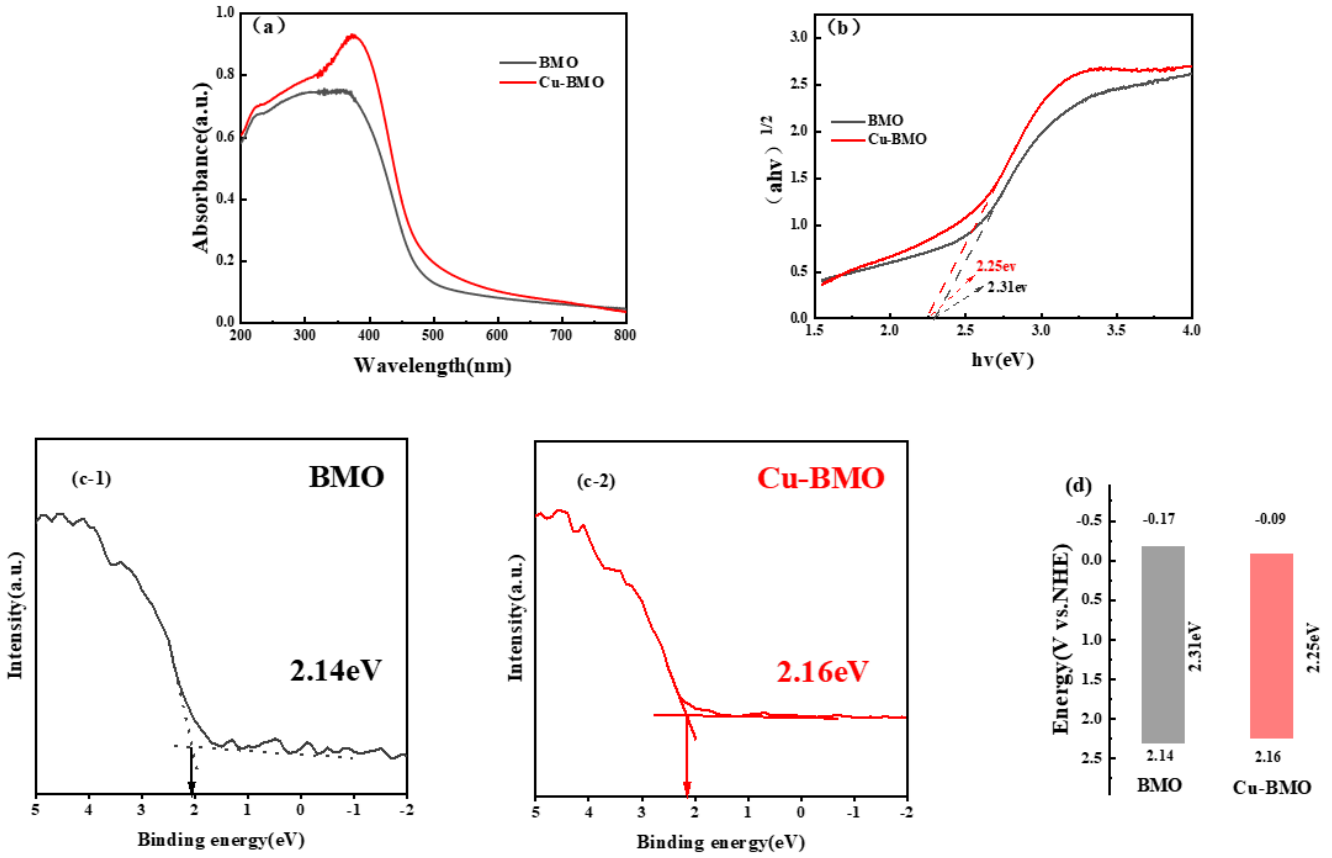


Figure 8

(a) UV-Vis spectra; (b) Tauc plots; (c) VB-XPS spectra; (d) Energy band diagrams.

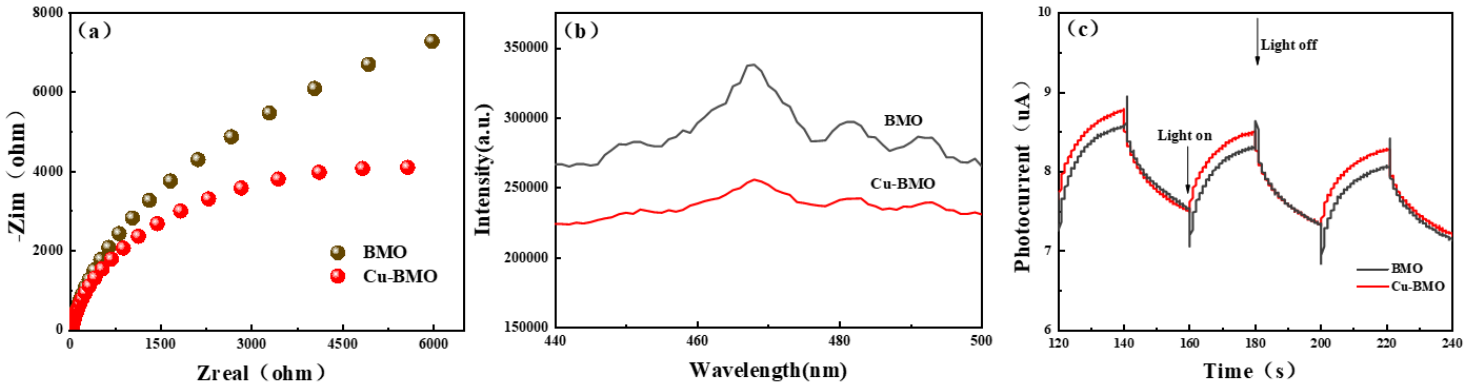


Figure 9

(a) EIS curves of the catalysts; (b) PL spectra of the catalysts; (c) photocurrent response curves.

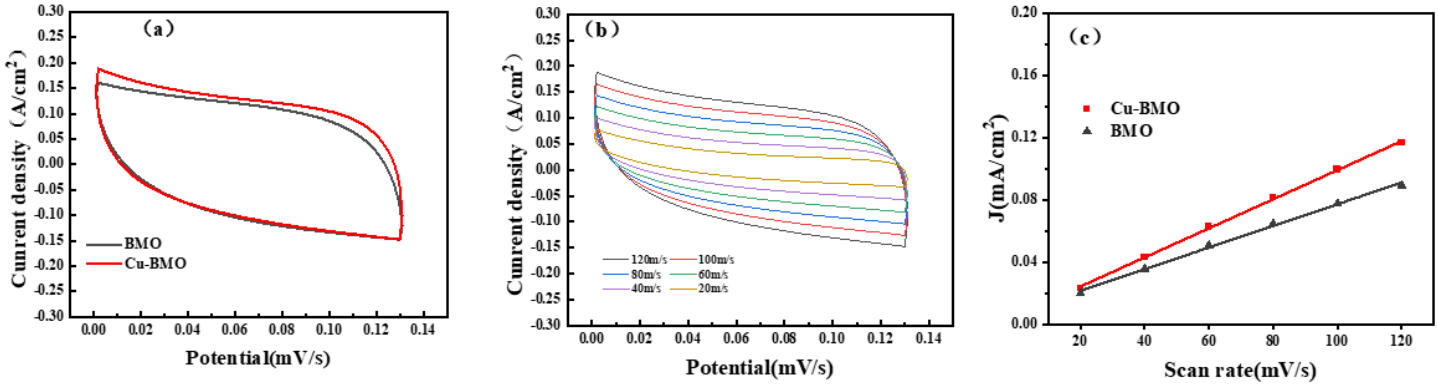


Figure 10

(a) CV curves of the catalysts; (b) CV curves of Cu-BMO at different scan rates; (c) ECSA curves.